BACHELOR

Effect of laser beam profile on the deformation of a tin droplet

Bras, Timo C.

Award date:
2018

Effect of laser beam profile on the deformation of a tin droplet

t.c.bras

August 2018
R-1950-SB

Abstract

By illuminating tin droplets with a laser beam the droplet will translate and deform as effect of a recoil interaction between a created plasma and the droplet. The use of spherical harmonics to approximate a pressure profile caused by a laser pulse on the droplet is an elegant way of determining the ratio between the deformation energy and the translation energy of the tin droplet. This method is used for theoretical laser beam profiles and simulated laser profiles. For Gaussian shaped laser profiles with an off set the off set seemed to only have a slight influence on the ratio between the translation and the deformation energy. When taking the limit of the pressure focus to zero, the asymptotic behaviour of the energy deformation energy was found to scale with the focus length with a negative third order dependency.

Contents

1 Introduction **4**

2 Physical problem formulation **5**

3 Mathematical problem **8**
3.1 General solution 8
3.2 Normalization of the boundary condition 9

4 Axi-symmetrical Gaussian laser pulses **11**
4.1 Method 11
4.2 Results 13

5 Analysis of experimental beam profile **16**
5.1 Experiment 16
5.2 Method 16
5.3 Results 16

6 Off centered laser impact **19**
6.1 Method 19
6.2 Results 20

7 Variations of laser profiles **23**
7.1 Two sided laser profiles 23
7.2 Ring focused laser profiles 23

8 Fully focused laser pattern **25**
8.1 Problem definition 25
8.2 Laplace equation on a half-space 25
8.3 Laplace equation on a sphere 26

9 Conclusion **33**

10 Discussion **33**

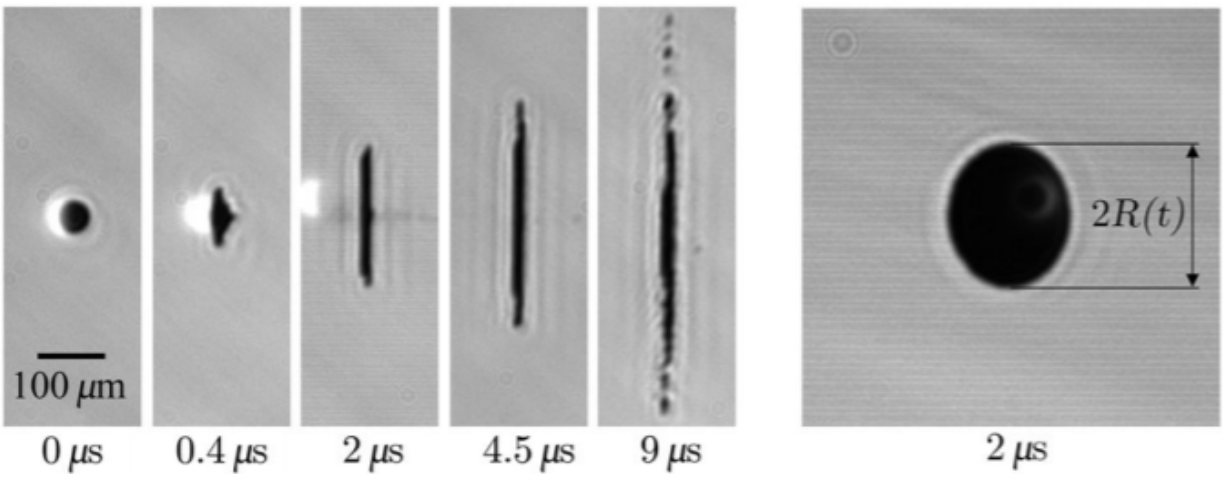

Figure 1: The plasma (white) as result of the laser pulse on the edge of a tin droplet (black) at 0 μs. The recoil of the tin droplet until it scattering from 0.4 μs to 9 μs. Due to the imaging techniques used for this image the white plasma from 0μs is still visible at 0.4 μs and 2 μs but is in reality no longer present at those time scales. Image taken from [6]

1 Introduction

The newest lithography machines of ASML use extreme ultraviolet (euv) light to create smaller structures in their chips. However the creation of euv light is a complex procedure that is not optimized yet. A short laser pulse is shot at a tin droplet in vacuum. This deforms and translates the droplet into a disk shape. This disk shape is then again shot at by a second laser pulse to transform the liquid tin into a plasma state. The tin plasma will then radiate the euv light that is used for the lithography [9].

To optimize the amount of euv light radiated after the second laser pulse the shape of the tin droplet is crucial. This shape is determined by the first laser pulse on the tin droplet. The first laser pulse will heat and ionize only a small fraction of the total tin droplet on the edge of the droplet into a plasma due to the small penetration depth of the laser. This plasma expands with a great velocity and will exercise a force on the rest of the droplet. This effect can be seen in Figure 1. Since the plasma is only on one side of the droplet the plasma will expand into one direction while pushing the rest of the droplet in the opposite direction. Due to this force of the plasma on the droplet the droplet will not only translate but also deform.

To be able to optimize the euv machine it is important to understand how this first laser pulse translates and deforms the tin droplet. In this report the influence of different laser profiles on the deformation and translation of the tin droplet right after the laser pulse is determined using a mathematical base of spherical harmonical functions.
The physical problem is dissected and made dimensionless in Chapter 2. Secondly this dimensionless problem is solved analytically in Chapter 3. After this is done the method is compared to a similar model[1] by calculating some basic pressure profiles by means of simulations in Chapter 4. Furthermore this method is used to give a better estimation of the energy distribution of simulations run in Chapter 5. This method is also used to give an estimate of the final expansion velocity of the tin droplet for off set Gaussian shaped laser profiles in Chapter 6. In Chapter 7 some less conventional laser profiles are looked at. Lastly the method is used to determine asymptotic behaviour for fully focused pressure profiles in Chapter 8.

2 Physical problem formulation

The time scales of the laser tin droplet interaction can be taken apart into three different order's of magnitude. The time scale in which the laser beam is active,t_l, and the time in which the plasma is created and recoils of the droplet,t_p, are both of order $t_l \approx t_p \approx 10^{-8}s$ [6]. This can be seen in Figure 2(a). The time scale of the translation and deformation of the droplet into a thin sheet,t_s is of order $t_s \approx 10^{-6}s$ [6]. This effect can be seen in Figure 2(b). This droplet when then deform into a thin sheet which will under go surface tension limited expansion Figure 2(c) with a time scale of $t_s t \approx 10^{-5}s$ [6] and after the she become unstable it will shatter Figure 2(d).
When the laser beam is active a thin layer at the laser side of the tin droplet is ionized into a plasma and will then absorb all of the laser energy. Due to this absorption the small layer of plasma will have a high energy and start to expand. Since the plasma is surrounded by liquid tin on one side and vacuum on the other side it will expand into the vacuum while due to the normal force between the tin droplet and the plasma. Due to the law of momentum conservation

$$MV_{cm} = mv_{cm} \ , \tag{1}$$

with m and M the mass of the droplet and plasma respectively and v_{cm} and V_{cm} the velocity of the centre of mass of the droplet and the plasma respectively.
The plasma droplet interaction can be modeled as a pressure profile that is exercised by the plasma on the droplet. The laser profile is however measured in intensity in $\frac{J}{m^2}$ whereas a pressure profile is in $\frac{N}{m^2}$ The exact conversion from the energy profile of the laser to the pressure exercised by the plasma on the droplet is a complex model dependent on many factors and plasma physics. However for the average of the pressure profile the following dependency has been found to fit for laser profiles of different energy's [7]:

$$p_{av} \propto E_{od}^{0.6} \quad , \tag{2}$$

with p_{av} the average pressure on the droplet during the active laser period and E_{od} the total laser energy that is absorbed by the droplet. Equation (2) is used to convert the intensity profiles of laser into pressure profiles.
Further more due to the difference in time order between the pressure profile created by the plasma and the time of deformation and translation of the droplet this pressure profile exercised by the plasma is on an almost perfect sphere. To determine the effect of this laser droplet interaction the Navier-Stokes Equation is solved on a sphere with the pressure profile on the sphere and a stationary droplet as the boundary conditions.

Navier-Stokes The Navier-Stokes equation is:

$$\frac{\partial v}{\partial t} + (v \cdot \nabla)v + \frac{1}{\rho}\nabla p = \nu \Delta v, \tag{3}$$

where v is the velocity of the fluid, t is the time, p is the pressure, ρ is the density of fluid and ν is the kinematic viscosity.

Besides that the assumption is made that the fluid is incompressible

$$\nabla \cdot v = 0 \tag{4}$$

To get a better feel of the components in Equation (3) the system is made dimensionless. This done using the following basic units from the system.

r_0 = Radius droplet ,v_{cm} =Velocity of the center of mass of the droplet
t_0 = Time in which the pressure field acts upon the droplet ,ρ =The mass of the droplet

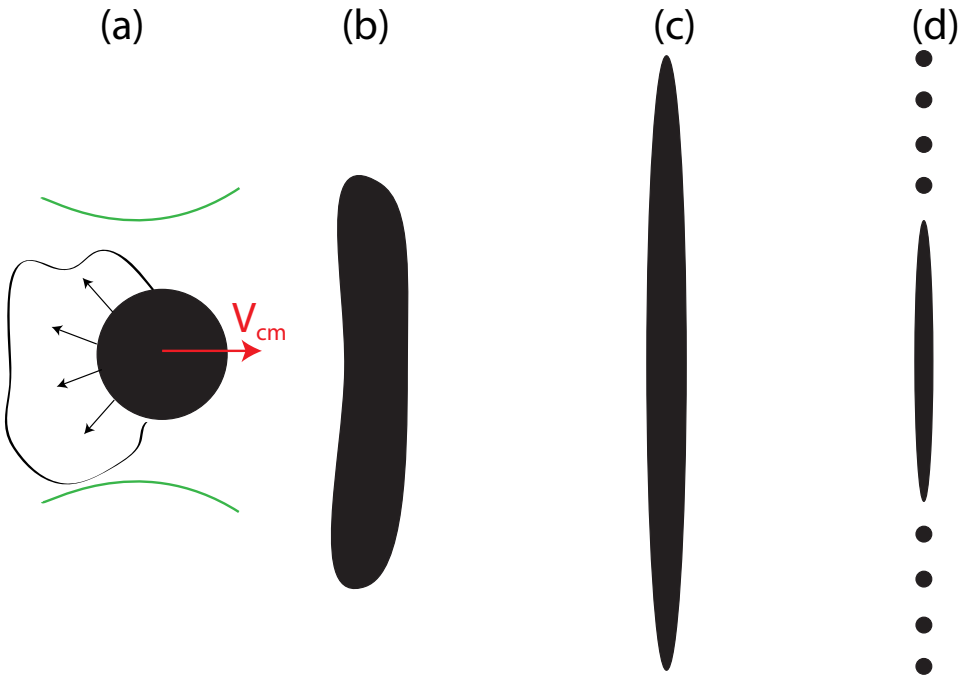

Figure 2: The four stages of the laser droplet interaction. (a) The laser is active and the plasma recoils on the droplet. (b) The initial deformation stage (c) The thin sheet surface tension-limited expansion (d) The shattering of the thin sheet. Image taken from [1]

This gives the following dimensionless units:

$$v^* = \frac{v}{v_{cm}} \qquad ,\nabla^* = \nabla r_0 \qquad ,\Delta^* = \Delta {r_0}^2$$
$$t^* = \frac{t}{t_0} \qquad ,p^* = p\frac{t_0 {r_0}^2}{m_0 v_{cm}}$$

To nondimensionalize p^* the total momentum exchange between the droplet and the plasma is determined as $m_0 v_{cm}$ and the surface size on which this momentum exchange takes place scales with r_0^2 and the time this pressure field is active scales with t_0.

Upon nondimensionalization, Equation (3) reads:

$$\frac{\partial v^*}{\partial t^*} T + (v^* \nabla^*) v^* + \nabla^* p^* T = \Delta^* v^* \frac{1}{Re} \tag{5}$$

With $Re = \frac{v_{cm} r_0}{\nu}$ and $T = \frac{r}{t_0 v_{cm}}$. Since $Re \approx 10^3$ and $T \approx 10^2$ the second and last term of Equation (5) can be neglected. This means that the viscous forces and the forces due to the velocity gradient are not significant for this problem. This gives an easier to solve approximation of the Navier-Stokes:

$$\frac{\partial v^*}{\partial t^*} \approx -\nabla p^*. \tag{6}$$

By taking the divergence of this equation it gives

$$\Delta p^* = 0 \tag{7}$$

since the divergence of v is equal to 0. This equation is one of the key equations to determine the pressure field over the droplet.

To determine the velocity profile of the droplet Equation (6) is integrated over the pressure pulse duration t_p. This integration gives:

$$v \approx -\frac{1}{\rho}\nabla \int_0^{t_p} p(\tau)d\tau = -\frac{t_p}{\rho}\nabla p, \tag{8}$$

$$v^* = \nabla \int_0^1 p(t)^* dt = \nabla p^*, \tag{9}$$

$$v^* = t_l \nabla p^*_{av} \tag{10}$$

with p the average pressure during the pulse.

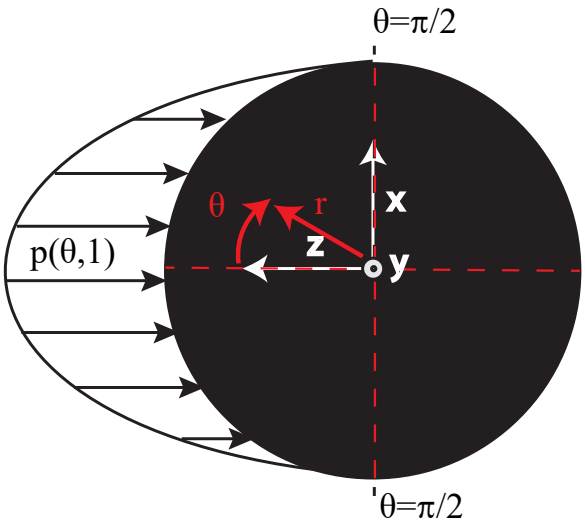

Figure 3: the pressure field on the tindroplet $p_e(\theta)$ as a function of the polar angle θ, the Cartesian and Spherical coordinate systems are shown in white and red respectively.

3 Mathematical problem

3.1 General solution

The physical problem of finding the response of a liquid drop to a laser pulse impact has now been translated into the solution of the Laplace equation for the pressure with a boundary condition on the sphere. From now on the problem is determined for the non dimensional problem and all the $*$'s are dropped.
For most problems in this report it is assumed that the problem is axisymmetric. This means that all properties in a concentric circle around a specific z-axis are equal. In this case the problem can be described using only two coordinates for space, namely the distance to the center, r and the angle between the z-axis and concentric circle, θ. For non-axisymmetric cases the azimuthale angle ϕ will be used.
The problem has been translated from a physics problem to a pure mathematical problem in Equation (6) and (7). The dimensionless variables are taken in such a way that the problem is on a sphere of radius 1 and the following equations have to hold:

$$\Delta p(r, \theta, \phi) = 0, \tag{11}$$

with a boundary condition $\overline{p}(\theta, \phi)$ such that

$$p(r, \theta, \phi) = \overline{p}(\theta, \phi). \tag{12}$$

The following problem has been solved before and the general solution [4] to this problem is

$$p(r, \theta, \phi) = \sum_{l=0}^{\infty} \sum_{m=-l}^{l} (A_l r^l + B_l r^{-l-1}) Y_l^m(\theta, \phi), \tag{13}$$

in which A_l and B_l are coefficients used to satisfy the boundary conditions and Y_l^m are the spherical harmonics. However since the problem is inside the sphere and must be bounded, all the factors B_l must be equal to zero else the solution is singular at $r = 0$. Furthermore the boundary condition can only be real which means that the entire solution can also only be real. Because of these two argument the general solution of will be

$$p(r,\theta,\phi) = \sum_{l=0}^{\infty} \sum_{m=0}^{l} r^l P_l^m(\cos(\theta)(S_l^m \sin(m\phi) + C_l^m \cos(m\phi)), \tag{14}$$

in which S_l^m and C_l^m are coefficients used to satisfy the boundary conditions and $P_l^m(\cos(\theta)$ are the legendre polynomials. Since the spherical harmonics form a complete orthonormal set, the coefficients S_l^m and C_l^m for a specific boundary condition are unique and can be determined by

$$S_l^m = \int_0^{\pi} \int_0^{2\pi} \overline{p}(\theta,\phi) P_l^m(\cos(\theta)) \sin(m\phi)) \sin(\theta) d\phi d\theta, \tag{15}$$

$$C_l^m = \int_0^{\pi} \int_0^{2\pi} \overline{p}(\theta,\phi) P_l^m(\cos(\theta)) \cos(m\phi)) \sin(\theta) d\phi d\theta. \tag{16}$$

When looking at axisymetrical boundary conditions the general solution becomes only depended on r and θ in the following way

$$p(r,\theta) = \sum_{l=0}^{\infty} A_l r^l P_l^m(\cos(\theta), \tag{17}$$

with coefficient A_l is determined by:

$$A_l = 2\pi \int_0^{\pi} \overline{p}(\theta) P_l^0(\cos(\theta) \sin(\theta) d\theta. \tag{18}$$

Now that the pressure profile is determined, the velocity can also be calculated using Equation (10). The velocity, v,is calculated at each point in the spherical droplet using

$$v(r,\theta,\phi) = -\nabla p(r,\theta,\phi). \tag{19}$$

One of the properties that are interesting for the deformation problem of the droplet is the total deformation energy and the translation energy. To be able to determine the deformation energy of the droplet the total kinetic energy is important. The total kinetic energy, E_{kin} is equal to

$$E_{kin} = \int_0^1 \int_0^{2\pi} \int_0^{\pi} (\nabla p(r,\theta,\phi))^2 r^2 \sin(\theta) d\theta d\phi dr. \tag{20}$$

The total deformation energy E_{def} will be equal to

$$E_{def} = E_{kin} - E_t, \tag{21}$$

with E_t the total translation energy.

3.2 Normalization of the boundary condition

To be able to compare different boundary conditions they need to be normalized in one way or another. This is done by normalizing the total momentum given to the sphere. So if $\overline{p}(\theta)$ is a non normalized axisymetric boundary condition itsmomentum will be equal to itsmomentum in the $\overline{e}_z$ direction since the $\overline{e}_x$ and $\overline{e}_y$ direction are cancelled out due to the symmetry. itsmomentum $|M|$ will be equal to

$$|M| = |M_{\overline{e}_z}| = \int_0^{\pi} \int_0^{2\pi} \overline{p}(\theta,\phi) \sin(\theta) \cos(\theta) d\phi d\theta \tag{22}$$

and

$$\widetilde{p}(\theta,\phi) = \frac{\overline{p}(\theta,\phi)}{M}. \tag{23}$$

For non axi-symetrical problems the momentum M can be determined by calculating

$$|M| = \sqrt{M_{\bar{e}_x}^2 + M_{\bar{e}_y}^2 + M_{\bar{e}_z}^2}. \tag{24}$$

Using this normalization the moment will be equal to 1. So the translation energy of the center of mass of the droplet can be calculated as

$$E_t = \frac{1}{2}\frac{M^2}{m} = \frac{3}{4\pi}, \tag{25}$$

with M the total momentum and m the mass of the droplet. Since all properties have been made dimensionless the mass of the droplet is equal to itsvolume. So $m = \frac{4\pi}{3}$.

4 Axi-symmetrical Gaussian laser pulses

4.1 Method

To get a basic idea of how different pressure profile act upon a tin droplet a few different pressure profiles are tested using the mathematical method from the previous section. First of all the assumption is made that the shape of the pressure profile is identical to the shape of the energy profile of the laser or can be converted using Equation (2). This is done to simplify the complex plasma physics that occur at the interface of the droplet during the laser impact. The standard laser profiles are a top hat profile which is an beam with equal intensity all around. And a Gaussian shaped intensity profile. For the laser profiles the coordinate system seen in Figure 3 is used with the laser coming from the positive z-direction.

1. A top hat pressure profile that puts an even force per area in the xy surface.
   Due to the curvature of the sphere the total energy per unit of surface scales with $\cos\theta$ and for $\theta > \frac{\pi}{2}$ the surface is on the side the laser can not reach. So the pressure profile is equal to

$$\overline{p}(\theta) = H(\frac{\pi}{2} - \theta)\cos\theta, \tag{26}$$

   with H the Heaviside function.

2. A Gaussian pressure profile over the polar coordinate of the sphere.
   A Gaussian shaped intensity profile is directly converted into the pressure profile. The plasma is assumed to even pressure the droplet from the side the laser can not reach a little bit. This gives

$$\overline{p}(\theta) = e^{\frac{\theta^2}{2\sigma^2}}. \tag{27}$$

3. A Gaussian pressure profile on the xy surface coming from the positive z direction.

$$\overline{p}(\theta) = H(\frac{\pi}{2} - \theta)e^{\frac{\sin(\theta)^2}{2\sigma^2}}\cos(\theta) \tag{28}$$

4. A Gaussian pressure profile on the xy surface coming from the positive z direction corrected for the energy to pressure conversion from Equation (2).

$$\overline{p}(\theta) = H(\frac{\pi}{2} - \theta)e^{\frac{\sin(\theta)^2}{2\sigma^2}}\cos(\theta))^{0.6} \tag{29}$$

This gives to following axisymmetric pressure profile formula's:

Since all these formulas are axisymmetric the azimuthal spherical harmonics will have a coefficient of 0. Therefor the pressure profiles over the entire sphere will look like

$$p(\theta, r) = \sum_{l=0}^{\infty} A_l r^l P_l^0(\cos(\theta)) \tag{30}$$

The solutions are calculated numerically using Mathematica. A cut off has to be made for the number of spherical harmonics used. This is done by

$$p(\theta, r, l_{max}) = \sum_{l=0}^{l_{max}} A_l r^l P_l^0(\cos(\theta)), \tag{31}$$

with l_max the cut off point. To decide a cut off of the number of spherical harmonics the following error measurement is used

$$Er(l_{max})\frac{\int_0^{\pi}\int_0^{2\pi} |P(\theta, r, l_{max}) - overline p(\theta)|\sin(\theta)d\phi d\theta}{\int_0^{\pi}\int_0^{2\pi} \overline{p}(\theta)\sin(\theta)d\phi d\theta}. \tag{32}$$

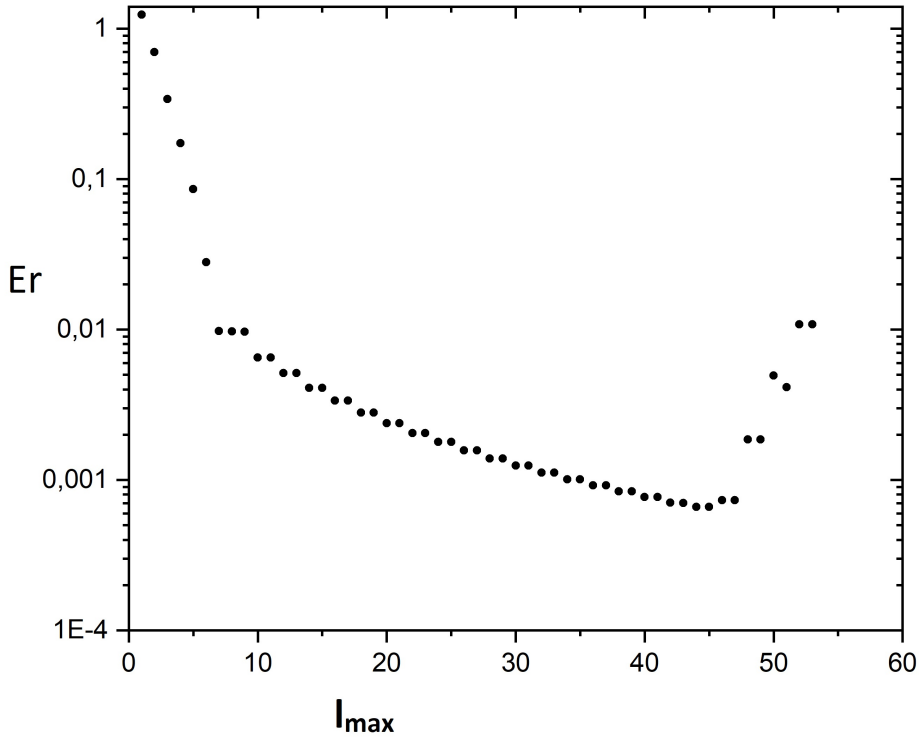

Figure 4: Er as function of number of spherical harmonics l_{max} for $\overline{p}(\theta) = e^{\frac{\sin(\theta)^2}{2\sigma^2}} \cos(\theta) H[\frac{\pi}{2} - \theta]$

This coefficient show the relative error between the real pressure boundary condition and the series approximation. It should approach zero for a correct estimate of the pressure profile.

Due to the highly oscillating nature of the higher order spherical harmonics the standard numerical integrating techniques will make significant errors when calculating the coefficients. In Figure 4 the relative error declines for higher values of l_max up until around 50. For $l > 50$ the standard Mathematica calculations become inaccurate. In the rest of this report

$$l_{max} = 40 \tag{33}$$

and

$$Error(l_{max}) < 0.01 \tag{34}$$

unless stated otherwise.

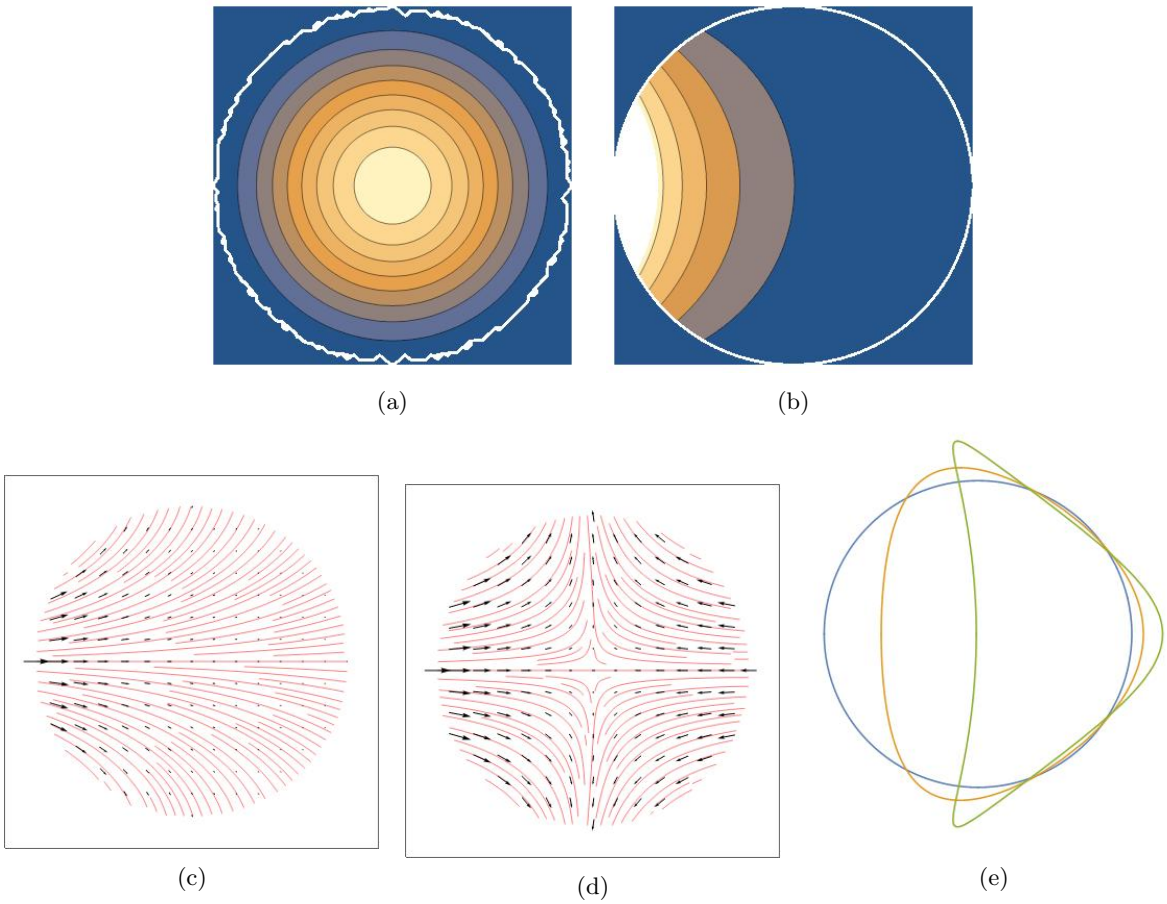

Figure 5: Pressure distribution and movement of a droplet as effect of a gaussian pressure pulse with a $\sigma = 0.5$. (a) The boundary condition seen at the edge of droplet in the xy plane with $z = \sqrt{1 - x^2 - y^2}$ (b) The pressure distribution on the xz-plane (c)The velocity profile on the xz-plane from a stationary perspective.(d)The velocity profile on the xz-plane from a co-moving perspective. (e) Approximation of the moving contour in the xz-plane.

4.2 Results

In this chapter the deformation of a tin droplet as a result of different laser profiles is investigated, in specific the laser profiles of Equation (26), (27), (28) and (29). The most important property that is looked at is the ratio between the kinetic energy of the droplet that is used to deform the droplet and the total kinetic energy. This ratio gives information not only about the direct deformation of the droplet but also for the surface tension limited expansion. To calculate this first the pressure profile over the entire sphere during the active laser period is determined. Using Equation (10) the velocity field is determined. Then the total kinetic energy and the deformation energy are calculated using Equations (20) and (21). In Figure 5 and Figure 6 the entire process from the boundary condition to the approximated movement of the contour of the droplet is shown. Comparing the two figures it can be seen that the more focused pressure profile in Figure 5 leads to more deformation of the droplet at the contour. The pressure distribution inside of the sphere is also more extreme with a high pressure at $\theta = 0$, the focus point, and a steep decline of pressure moving into the droplet. The ratio $\frac{E_{def}}{E_{kin}}$ is also higher for $\sigma = 0.5$ then for $\sigma = 1$.
This ratio is calculated for all laser profiles from Equation (26), (27), (28) and (29) and is shown in Figure 7. For highly focused laser profiles almost all of the energy goes into the deformation of the droplet whereas when having no focus this energy drops to around $\frac{1}{3}$ of the total energy and the droplet is more translated then deformed.

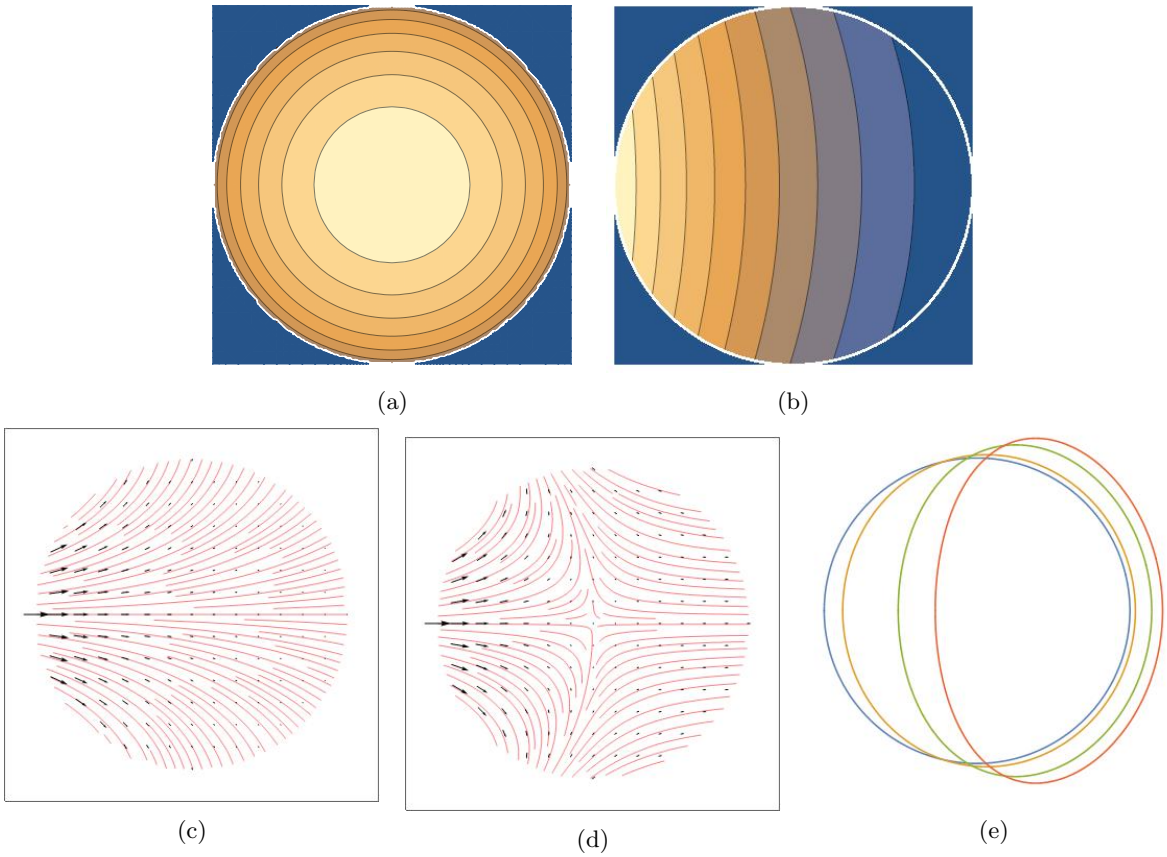

Figure 6: Pressure distribution and movement of a droplet as effect of a Gaussian shaped pressure pulse with a $\sigma = 1$. (a) The boundary condition seen at the edge of droplet in the xy plane with $z = \sqrt{1 - x^2 - y^2}$ (b) The pressure distribution on the xz-plane (c)The velocity profile on the xz-plane from a stationary perspective.(d)The velocity profile on the xz-plane from a co-moving perspective. (e) Approximation of the moving contour in the xz-plane.

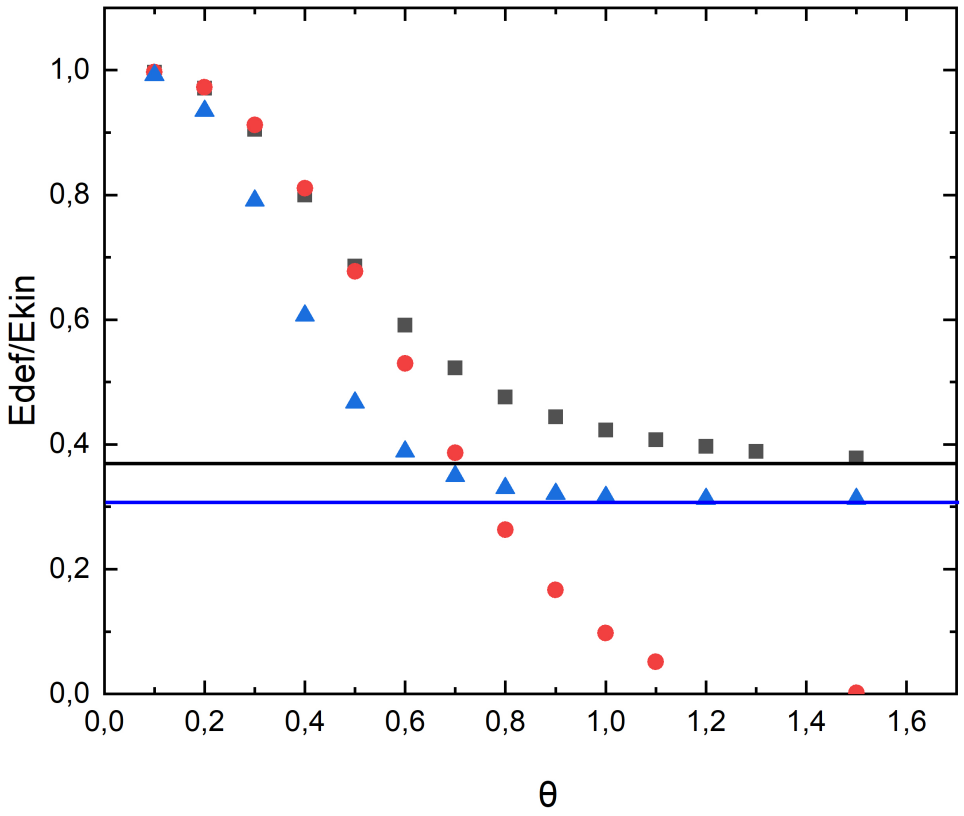

Figure 7: The energy distribution of a tin droplet after laser impact. Different Gaussian pressure profiles are used. Red: Gaussian distribution on curve, Black: gaussian pressure profile on xy-plane. Blue: gaussian pressure profile on xy-plane corrected with energy to pressure conversion. The black and blue lines represent the top hat and the top hat correct with the energy to pressure conversion respectively.

For the 3 Gaussian pressure profiles the ratio between the deformation energy and the total kinetic energy is determined. This is done for different focus lengths in figure 7. One clear thing that can be taken away from this figure is that focussing the pressure profile makes it so that the ratio of $\frac{E_{def}}{E_{kin}}$ rises.

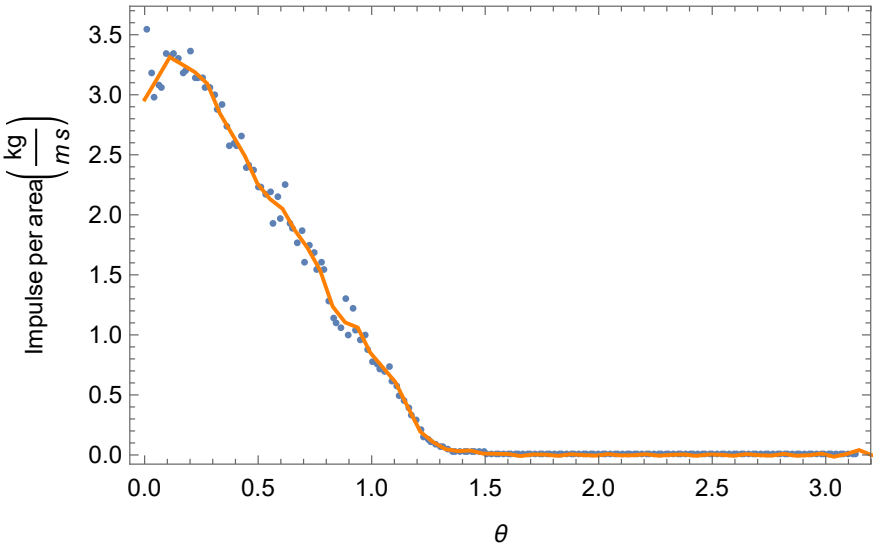

Figure 8: The symbols show the pressure profile of the ARCNL simulation of a 50μm laser with an energy of 80μJ on the droplet. The line is the approximation of the droplet using Equation (35) with $l_{max} = 50$

5 Analysis of experimental beam profile

5.1 Experiment

In the previous chapter the pressure profiles were equal to the energy profiles of the used laser's or using the exponential conversion from Equation (2). However the conversion from laser energy to pressure on the droplet is not just a local conversion from the laser energy to the pressure energy. At ARCNL computer simulations were done using RALEF-2D radiation-hydrodynamic code to determine the pressure profiles that were formed by the plasma around the tindroplet for different laser energies and laser focuses [5]. In these simulations the laser droplet interaction was modeled using a finite element method to determine the laser droplet plasma interaction. Out of these models the impulse on the spherical surface was determined for every degree of θ. This was done for laser beams with different energies and focus lengths.

5.2 Method

To determine the coefficient for the spherical harmonics the following sum based on Equation (18) was used, however the integral is replace by a sum since the given data is discrete:

$$A_l = \sum_{n=1}^{180} \overline{p}(n) Y_l(\frac{(n-\frac{1}{2})\pi}{180}) \sin(\frac{(n-\frac{1}{2})\pi}{180}) \frac{\pi}{180}. \tag{35}$$

the calculation of the momentum was done in a similar way as in equation 22. In Figure 8 a pressure profile and an approximation using spherical harmonics are shown. The error for these functions using spherical harmonics up to $l = 50$ is around $Er \approx 0.01$ and never exceeds 0.03.

5.3 Results

Using the data from simulations the energy ratio, $\frac{E_{def}}{E_{kin}}$ is determined. These results can be found in Figure 9. The same results as in Figure 7 is found, namely that the more focused the laser beam profile is the higher the deformation energy. A difference between the results from Figure 7 and from Figure 9 is the influence of the energy on the droplet. For Figure 7 the energy on droplet was irrelevant but for Figure 9 a higher energy on droplet means that the ratio energy ratio is lower. This can be explained by looking at the data from the simulation in which the pressure profile for higher laser energies is a lot more spread out as can be

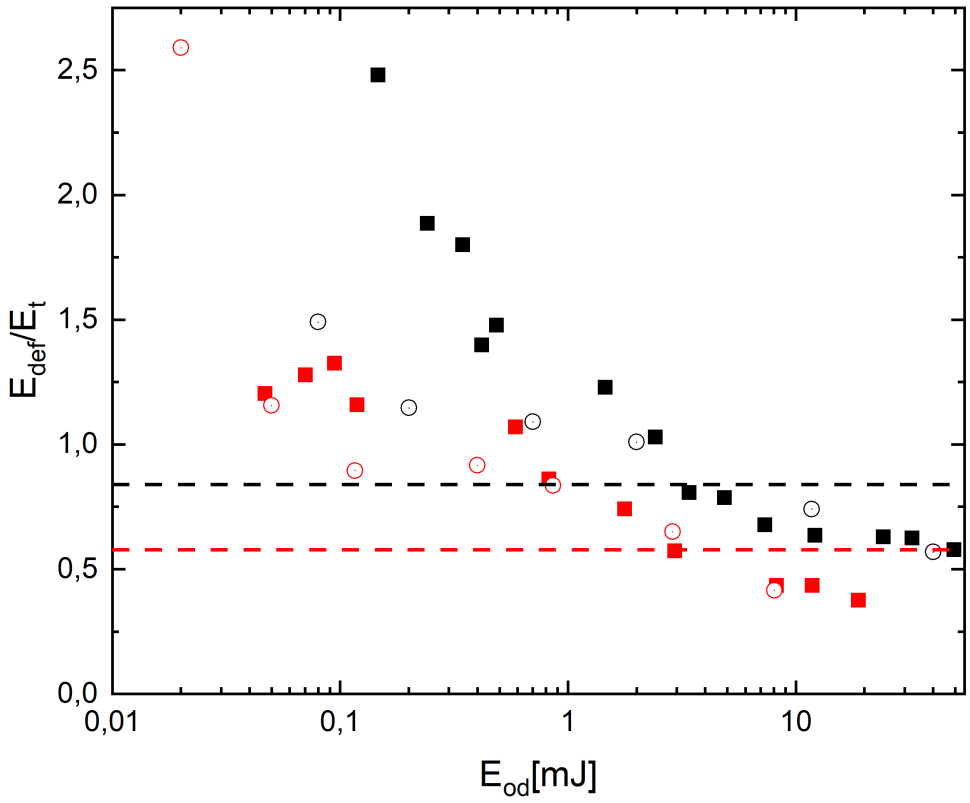

Figure 9: Energy ratio of a 50μm tin droplet for different laser energies and profiles. The pressure profiles are attained from ARCNL simulation. The full squares are data attained from ARCNL experiments. The black lines and points are for the Full Width Half Maximum (FWHM) of 50 μm and the red lines and points are for the FWHM of 115 μm. The full squares are experimental data. The circles show the energy distribution for different laser energies on the droplet and are determined by numerical approximations using the pressure profiles from the ARCNL simulations. The dashed line shows the energy distribution of a Gaussian pressure profile with a FWHM of 50μm and 115 μm on the xy-plane.

seen in figure 10. There is even a significant pressure on the backside of the droplet. This effect is caused by the size and shape of the plasma cloud which is a lot larger and more extended to the backside of the tin droplet for higher laser energies. This can be seen from experimental pictures in Figure 11.

The experimental data follow the same trends as the data from the simulations. For low E_{od} the deformation in the experiments is higher then the simulations predict but for higher E_{od} this is no longer the cases. It is interesting to note that around $E_{od} = 2mJ$ the energy ratio is equal for the simulations, experiments and the simplified Gaussian pressure profile with the same Full Width Half Maximum(FWHM) focus.

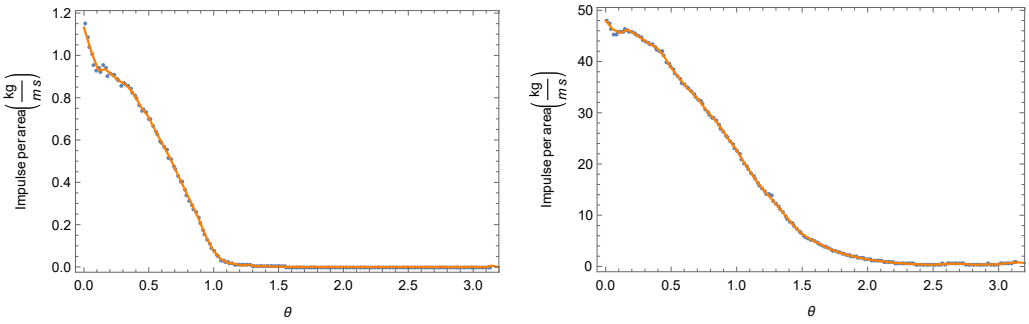

(a) (b)

Figure 10: The pressure profile of two laser but with a FWHM of 115μm. (a) has a total energy of 20μJ ,(b) has a total energy of 8062μJ.

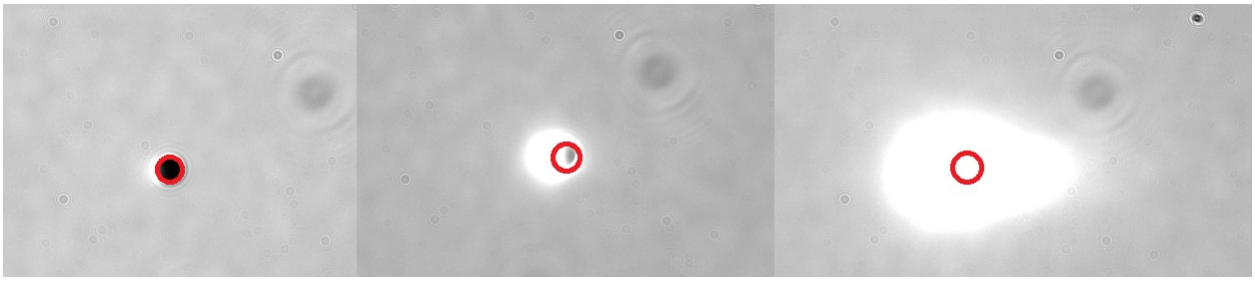

Figure 11: The plasma cloud (white) created by three different laser energies with the same focus. In red the size of the droplet is shown. The laser energies are 0.5J, 20mJ, 300mJ respectively. Picture taken from [8].

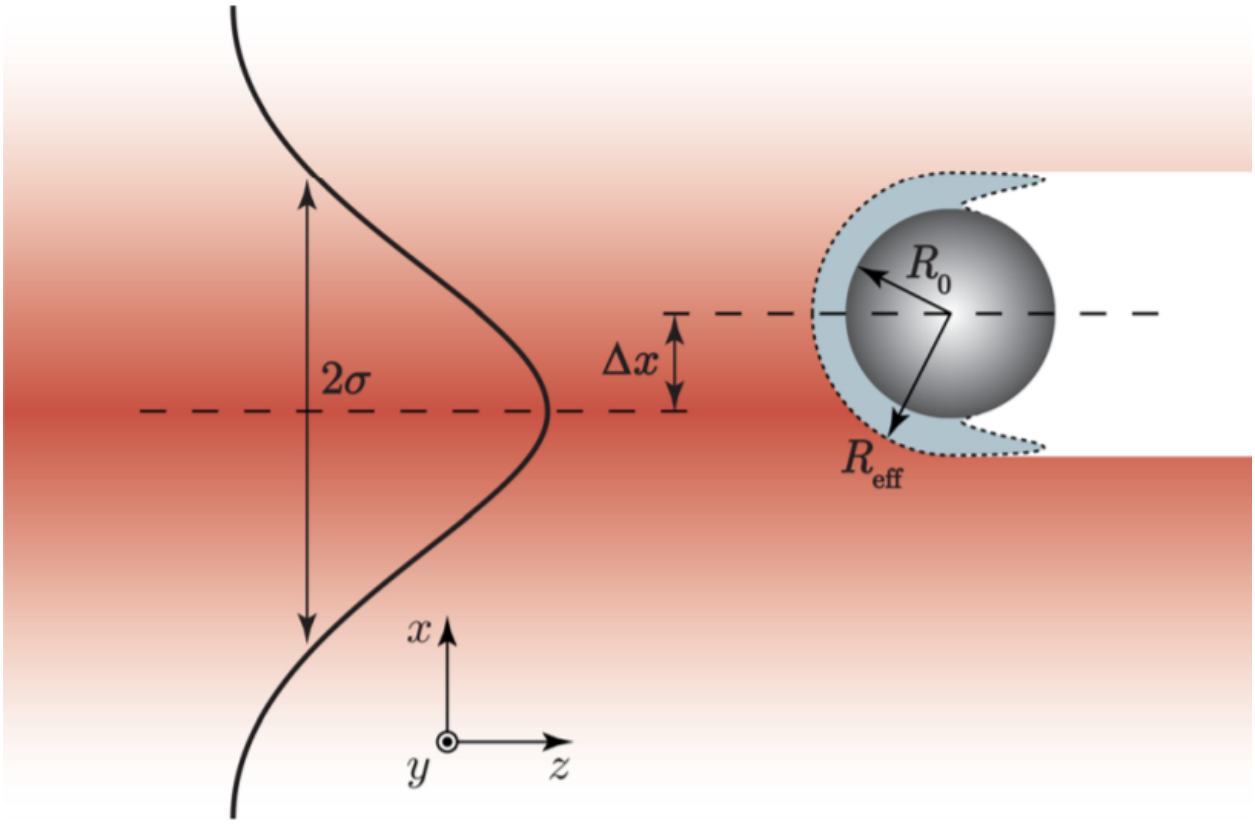

Figure 12: [3] Cross chapter of an off set Gaussian shaped laser profile on a droplet with an off set of Δx, The radius of the droplet is r_0 and the radius at which the plasma (light gray) absorbs the laser is equal to r_{eff}. Picture taken from [3]

6 Off centered laser impact

6.1 Method

In experiments the timing of the laser pulse to hit the tin droplet exactly in the centre has to be very precise. If this is not the case the tin droplet will be hit by a laser with an offset due to the fact that the tin droplet is moving. In this chapter the effect of hitting a tin droplet with an off set Gaussian laser on its deformation is determined. In Figure 12 the laser profiles is shown with an off set of Δx, a radius of r_0 and an effective radius that absorbs the laser energy of r_{eff}. The same Cartesian and spherical coordinate systems are used. In previous work [3] the assumption was made that the final expansion velocity has a linear relation with the velocity of the center of mass for equal laser profiles with different off sets:

$$\frac{\dot{r}(\Delta x)}{\dot{r}(0)} \propto \frac{v_{cm}(\Delta x)}{v_{cm}(0)} \tag{36}$$

However this does not take into account that an off set of the laser can change the distribution between translation and deformation energy. To accommodate for this the equation becomes

$$\frac{\dot{r}(\Delta x)}{\dot{r}(0)} \propto \frac{v_{cm}(\Delta x)}{v_{cm}(0)} \sqrt{\frac{E_{def}(\Delta x)}{E_{cm}(\Delta x)}} \sqrt{\frac{E_{cm}(0)}{E_{def}(0)}}. \tag{37}$$

and by using the relation $\sqrt{E_{cm}} \propto v_{cm}$ it gives.

$$\frac{\dot{r}(\Delta x)}{\dot{r}(0)} \propto \sqrt{\frac{E_{def}(\Delta x)}{E_{def}(0)}}. \tag{38}$$

For the calculation it is assumed that during the laser pulse the plasma cloud around the tin droplet will be of insignificant size and therefore $R_{\text{eff}} \approx R_0 = 1$. The equation of the offsetted pressure profile on the surface is:

$$\overline{p}(\theta,\phi) = (exp[\frac{\sin(\theta)^2 - 2\Delta x \sin(\theta)\cos(\phi) + \Delta x^2}{2\sigma^2}]\mathrm{H}(\frac{\pi}{2} - \theta)\cos(\theta))^{0.6} \tag{39}$$

or in Cartesian coordinates:

$$\overline{p}(x,y,z) = (exp[\frac{(x-\Delta x)^2 + y^2}{2\sigma^2}]\mathrm{H}(z)z)^{0.6}. \tag{40}$$

With $\sqrt{x^2+y^2+z^2} = r = 1$
Using Equation (15) and (16) the coefficients can be determined. Since the function is symmetric through the xz-plane the even functions cancel each other out so for all m and l: $S_l^m = 0$ .Furthermore for high values of m the numerical integration will converge very slowly due to the highly oscillatory behavior of the spherical harmonics with a high m value. Therefore they will not be accurate. To counter this problem with high values for m, the coordinate system is tilted over an angle c in the xz-plane such that

$$\overline{p}(0,0) = \text{Max } \overline{p} \tag{41}$$

and the highly oscillatory factor's will be smaller since the function is now centered around its maximum. Therefor the spherical harmonics for high m can be neglected in the approximation.

$$x = r(\cos(c)\sin(\theta)\cos(\phi) + \sin(c)\cos(\theta))$$

$$y = r\sin(\theta)\sin(\phi)$$

$$z = r(\sin(c)\sin(\theta)\cos(\phi) + \cos(c)\cos(\theta))$$

Filling this in for Equation (40) gives the function $\overline{p}(\theta,\phi)$ in the tilted coordinate system.

6.2 Results

The simulations that are run were for

$$\sigma = [0.5, 1, 2] \qquad \text{and } \Delta x = [0, 1, 2]. \tag{42}$$

In Figure 13 the approximation of the boundary condition is shown. The shifting of color after $\theta > \frac{\pi}{2}$ is only due to oscillatory behaviour with a small amplitude. As can be seen in the Figure the approximation using spherical harmonics is not exactly the same as the real boundary condition. Adding more coefficients would make them approach better but this would take a lot more computation time and power.

In Figure 14 the energy ratio can be seen for the Conditions 42. THe ratios do not depend a lot on Δx meaning that equations 39 and 37 are nearly the same. However the factor E_{def} becomes slightly more significant in the energy ratio for a larger off set. For the run simulations

$$1 \leq \sqrt{\frac{E_{def}(\Delta x)}{E_{cm}(\Delta x)}}\sqrt{\frac{E_{cm}(0)}{E_{def}(0)}} \leq 1.1. \tag{43}$$

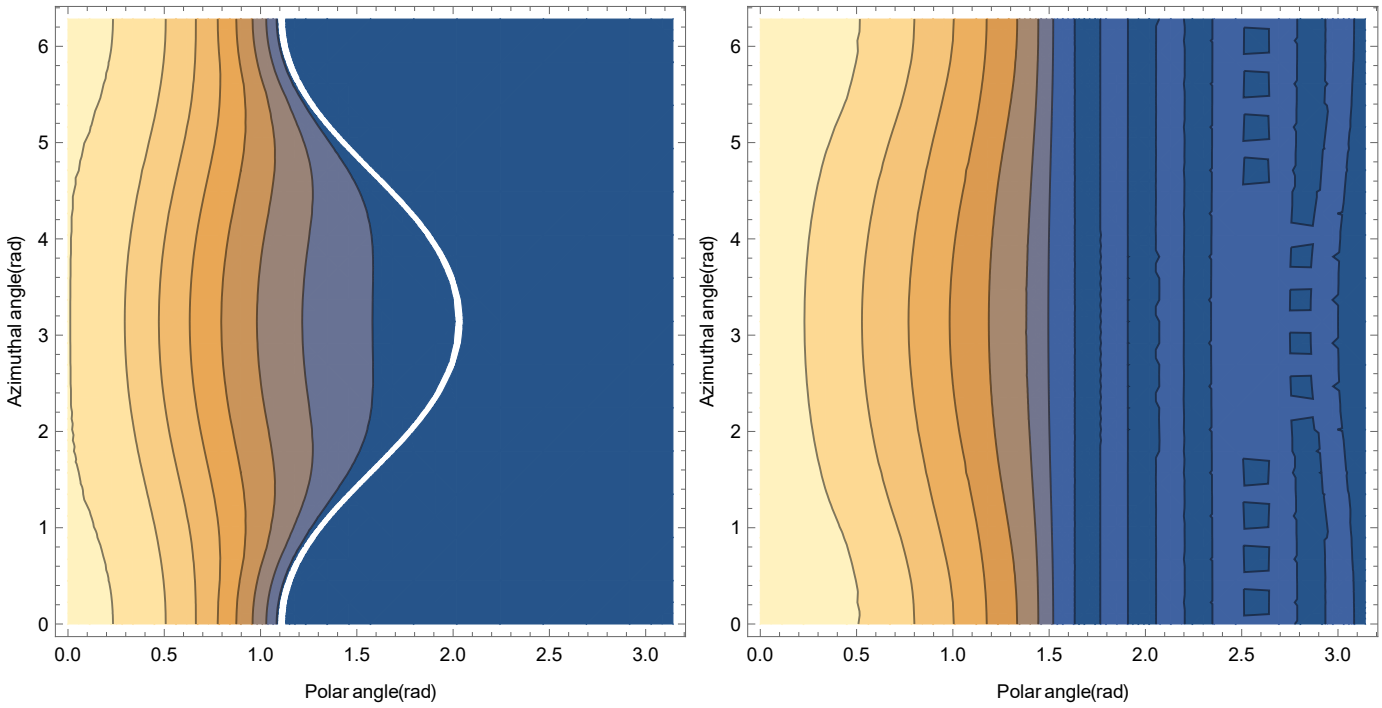

(a) (b)

Figure 13: The pressure profile of over the entire sphere is shown with tilted angle of 0.46 rad in the xz-plane. In (a) the exact boundary condition is shown for $\Delta x = 1$ and $\sigma = 1$, the white line is marks the non radiated part of the droplet. In (b) the approximation of (a) using Equation (14) with $l_{max} = 15$ and $m_{max} = 3$ is shown.

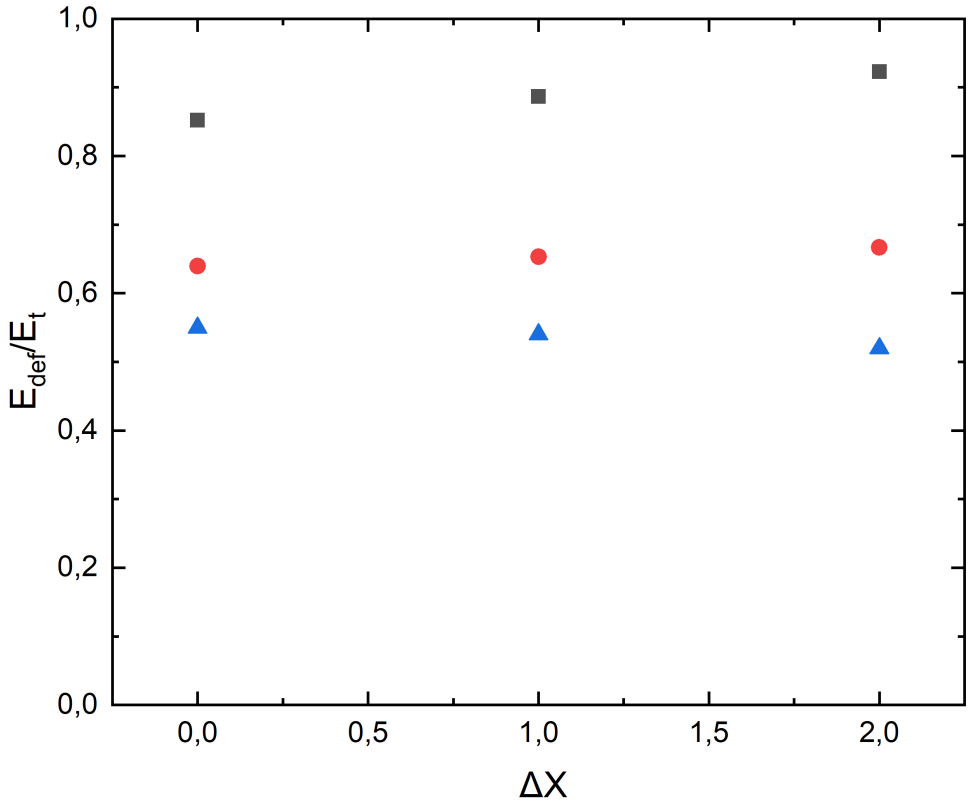

Figure 14: The ratio $\frac{E_{def}}{E_{kin}}$ for different Gaussian laser profiles with $\sigma = 0.5$, $\sigma = 1$ and $\sigma = 2$ in black, red and blue respectively

7 Variations of laser profiles

The laser profiles that are used to deform a tin droplet don't necessarily have to be Gaussian or top hat. By using beam manipulating or multiple laser's at the same time interesting beam profiles can be created. In this chapter some of those possibilities are discussed.

7.1 Two sided laser profiles

One of the possible changes in the setup is shooting a laser pulse from both sides of the tin droplet. One of the effects of this will be that their will be no translation of the droplet since their is now not only axis symmetry but also symmetry in the xy-plane. Because of this all the kinetic energy will go into the deformation of the droplet and the ratio $\frac{E_{def}}{E_{kin}} = 1$. The pressure profile used to simulate this behaviour is Equation 28 but mirrored so that

$$\overline{p}(\theta) = \cos\theta(H[\frac{\pi}{2} - \theta]e^{\frac{\sin\theta^2}{2\sigma^2}} + H[-\frac{\pi}{2} + \theta]e^{\frac{-\sin\theta^2}{2\sigma^2}}) \tag{44}$$

In Figure 15 the effect this laser profile has on the droplet is shown for $\sigma = 0.25$ and $\sigma = 0.7$. What can be seen is even though the pressure distribution through the droplet is vastly different the velocity profile and approximation of the contour movement are quite similar. Due to the linearity of the spherical coordinates a comparison can easily be made between the velocity vector's of the two laser Gaussian profile, v_2 and the single Gaussian laser profile v_1 as:

$$v_2(\theta, \phi, r) = v_1(\theta, \phi, r) + v_{1_x}(\pi - \theta, \phi, r)e_x + v_{1_y}(\pi - \theta, \phi, r)e_y - v_{1_z}(\pi - \theta, \phi, r)e_z \tag{45}$$

with $v_{1_{x,y,z}}$ the velocity in the respective direction. The total deformation energy for the two lasers Gaussian profile is equal to the deformation energy of two times At $\theta = \frac{\pi}{2}$ the droplet will only move in the x and y direction with

$$v_2(\frac{\pi}{2}, \phi, r) = 2(v_{1_x}(\frac{\pi}{2}, \phi, r)e_x + v_{1_y}(\frac{\pi}{2}, \phi, r)e_y). \tag{46}$$

Because of this the expansion rate at the equator ($\frac{\pi}{2}$) of the droplet is twice the expansion rate for a single Gaussian shaped laser profile.

7.2 Ring focused laser profiles

Another alternative laser profile would be a donut focused profile. This could give a pressure profile equal to

$$\overline{p}(\theta) = H[\frac{\pi}{2} - \theta]e^{\frac{\sin\theta^2}{2\sigma^2}}\cos\theta\sin\theta \tag{47}$$

In Figure 16 this profile is shown. Some interesting notions is that due to the fact that their is no pressure at $\sigma = 0$ the droplet will move outwards at $\sigma = 0$. The contour movement that is created as a result of the velocity profile becomes more triangular. This could be used when a a thick middle of the droplet is necessary to keep the structure stable. This is something that has not yet occurred at other pressure profiles.

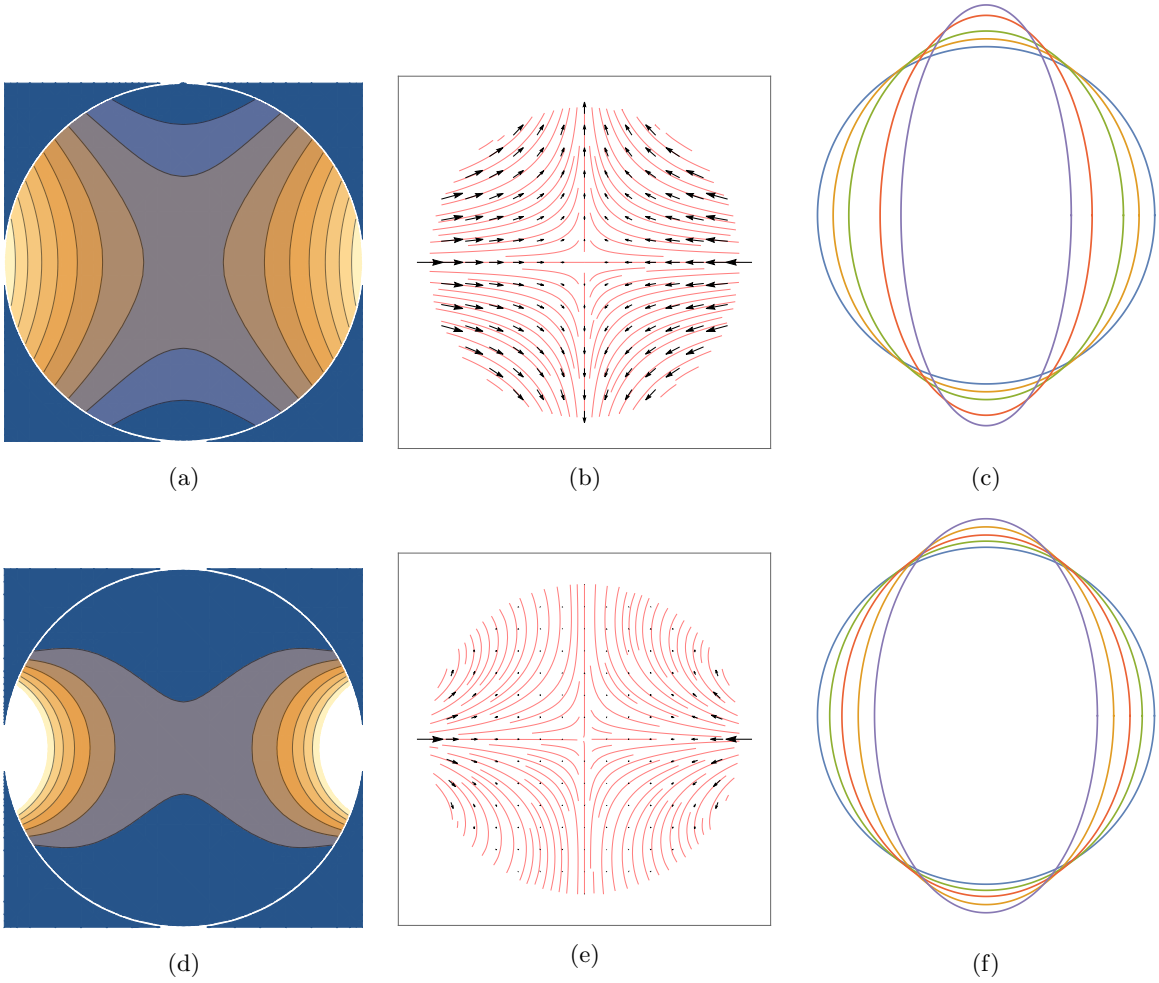

Figure 15: Two sided laser droplet interaction with boundary condition Equation (44) with $\sigma = 0.5$ for (a)(b)(c) and $\sigma = 1$ for (d)(e)(f).
(a)(d) The pressure distribution on the xz-plane (b)(e)The velocity profile on the xz-plane.
(c)(f) Approximation of the moving contour in the xz-plane.

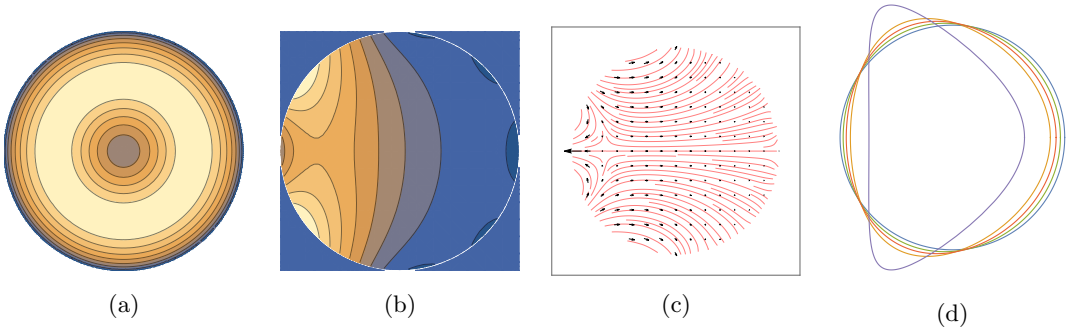

Figure 16: The laser droplet interaction for a donut shaped boundary condition from Equation (47)
(a) The boundary condition seen at the edge of droplet in the xy plane with $z = \sqrt{1 - x^2 - y^2}$
(b) The pressure distribution on the xz-plane (c)The velocity profile on the xz-plane as seen from a co-moving perspective. (d) Approximation of the moving contour in the xz-plane.

8 Fully focused laser pattern

8.1 Problem definition

When the laser is fully focused to one infinite small spot on the tin droplet all the energy of the laser will go into the deformation of the droplet as can be seen in Figure 7. In the next chapter we will look with more detail at the behaviour of the solution in the limit of infinitely small focus, $\sigma -> 0$. To this end two different geometries are used. is found using dimension analysis, with σ the focus length of the laser. In this report a closer look is taken on this behaviour using two different geometries. The first geometry that is looked at is a half space. This is done under the assumption that when a laser focus approaches zero on a sphere the critical space in which almost all the energy will be in a volume that scales with σ^3 and the curvature of the tin droplet will no longer be relevant to the problem. The second geometry that is looked at is a full sphere in which the mathematics of the problem become more advanced. In the end the same asymptotic behaviour is found as in [1].

8.2 Laplace equation on a half-space

In this chapter the scaling of solutions of the Laplace equation on a half space are determined. In particular the behaviour of the gradient of the solutions, the squared gradient and the double integral over x and y at $z = 0$ is determined. This is done since the gradient gives information of the acceleration of the fluid and the double integral gives information of the force applied to the fluid.
Consider the functions

$$u : \mathbb{R}^2 \times (0, \infty) \tag{48}$$

and

$$\kappa : \mathbb{R}^2 \tag{49}$$

with κ a function in L^2 in R^2.
Consider the following scaled functions

$$\overline{u}(cx, cy, cz) = u(x, y, z) \ , \tag{50}$$

$$\overline{\kappa}(cx, cy) = \kappa(x, y) \ , \tag{51}$$

with c as scaling factor.

Since u is a harmonic function and $\overline{u}$ is a linear scaling of u, $\overline{u}$ is also harmonic and satisfies Condition (50) . Furthermore

$$\overline{u}(x, y, 0) = u(\frac{x}{c}, \frac{y}{c}, 0) = \kappa(\frac{x}{c}, \frac{y}{c}) = \overline{\kappa}(x, y),$$

so $\overline{u}$ and $\overline{\kappa}($ also satisfy Condition (51).

Now these relations are used to determine the integral of $\overline{\kappa}(x, y)$ over x and y. This gives:

$$\int_{-\infty}^{\infty}\int_{-\infty}^{\infty} \overline{\kappa}(x, y) \ dxdy = \int_{-\infty}^{\infty}\int_{-\infty}^{\infty} \kappa(\frac{x}{c}, \frac{y}{c}) \ dxdy \ .$$

Set $\widetilde{x} = \frac{x}{c}$ and $\widetilde{y} = \frac{y}{c}$. Now: $dx = c \ d\widetilde{x}$ and $dy = c \ d\widetilde{y}$. Using this substitution changes the integral into:

$$\int_{-\infty}^{\infty}\int_{-\infty}^{\infty} \overline{\kappa}(x, y) \ dxdy = \int_{-\infty}^{\infty}\int_{-\infty}^{\infty} c^2\kappa(\widetilde{x}, \widetilde{y}) \ d\widetilde{x}d\widetilde{y}$$

so

$$\int_{-\infty}^{\infty}\int_{-\infty}^{\infty} \overline{\kappa}(x, y) \ dxdy = c^2 \int_{-\infty}^{\infty}\int_{-\infty}^{\infty} \kappa(x, y) \ dxdy \ . \tag{52}$$

For the gradient of $\overline{u}$ the following holds:

$$\frac{\partial}{\partial x}\overline{u}(x, y, z) = \frac{\partial}{\partial x}u(\frac{x}{c}, \frac{y}{c}, \frac{z}{c}) = \frac{1}{c}\frac{\partial}{\partial \widetilde{x}}u(\widetilde{x}, \frac{y}{c}, \frac{z}{c}) \ .$$

For the y and z derivatives analogously the same holds, therefore

$$\nabla\ \overline{u}(x_1, y_1, z_1) = \frac{1}{c}\nabla u(\frac{x_1}{c}, \frac{y_1}{c}, \frac{z_1}{c})\ . \tag{53}$$

When keeping the total force on the fluid equal but scaling the boundary condition $\kappa($ the function $\overline{\kappa}($ must be multiplied with $\frac{1}{c^2}$ to normalize its double integral as can be seen in Equation (52). Set

$$\widetilde{\kappa} = \frac{1}{c^2}\overline{\kappa}\ ,\ \widetilde{u} = \frac{1}{c^2}\overline{u}\ . \tag{54}$$

This gives for the gradient of $\widetilde{u}$ by combining Equation (53) and (54):

$$\nabla\ \widetilde{u}(x, y, z) = \frac{1}{c^3}\nabla u(\frac{x}{c}, \frac{y}{c}, \frac{z}{c}) \tag{55}$$

The following property that is looked at is the integral over the entire half space of $(\nabla\widetilde{u})^2$. So

$$\int_0^\infty \int_{-\infty}^\infty \int_{-\infty}^\infty (\nabla\widetilde{u}(x, y, z))^2\ dxdydz = \int_0^\infty \int_{-\infty}^\infty \int_{-\infty}^\infty \frac{1}{c^6}(\nabla u(\frac{x}{c}, \frac{y}{c}, \frac{z}{c}))^2\ dxdydz$$
$$= \frac{1}{c^3}\int_0^\infty \int_{-\infty}^\infty \int_{-\infty}^\infty (\nabla u(\widetilde{x}, \widetilde{y}, \widetilde{z})^2\ d\widetilde{x}d\widetilde{y}d\widetilde{z}$$

8.3 Laplace equation on a sphere

In the following chapter scaled solutions of the Laplace equation on a sphere are determined. In particular the behaviour of the gradient of the solutions is looked at for the same reason as in the previous section. The Laplace equation on a sphere is as following:
The function $p(r, \phi, \theta)$ will have to satisfy the following conditions:

$$\Delta p(r, \phi, \theta) = 0\ , \tag{56}$$

$$u(1, \phi, \theta) = \kappa(\phi, \theta, t)\ . \tag{57}$$

The general solution to Equation (56) is equal to Equation (13

$$p(r, \phi, \theta) = \sum_{l=0}^{\infty}\sum_{m=0}^{l}(A_l r^l + B_l r^{-l-1})Y_l^m(\theta, \phi) \tag{58}$$

and with azimuthal symmetry and the condition that the solution must be real and also be harmonic at $r = 0$, the general solution is

$$p(r, \theta, \phi) = \sum_{l=0}^{\infty} A_l r^l P_l(\cos(\theta))\ . \tag{59}$$

However the scaling of the boundary condition on a sphere is not as easy as for the half space. To be able to find a correct scaling parameter for the boundary condition on the surface of the sphere the heat transfer problem is used. For the half plane the conditions are

$$\frac{\partial\kappa}{\partial t} = \frac{\partial^2\kappa}{\partial x^2}\kappa + \frac{\partial^2\kappa}{\partial y^2}\kappa \tag{60}$$

$$\kappa(x, y, 0) = \kappa(_0(x, y) = \delta(x)\delta(y)\ , \tag{61}$$

with the general solutions as

$$\kappa(x, y, t) = \frac{1}{4\pi t}e^{\frac{x^2+y^2}{4t}}. \tag{62}$$

Now

$$\kappa(x,y,1) = \frac{1}{\sqrt{t}^2}\kappa(\frac{x}{\sqrt{t}},\frac{y}{\sqrt{t}},\sqrt{t}), \tag{63}$$

which is the same scaling that was used in the previous section. However the scaling variable has been replaced by $\sqrt{t}$. This replacement means that in the heat transfer problem the variable $\sqrt{t} = c$. This is useful since this is a scaling that can be translated to a sphere.

The boundary conditions on a sphere $\kappa($ have the following conditions:

$$\frac{\partial\kappa(\phi,\theta,t)}{\partial t} = \Delta_s\kappa(\phi,\theta,t) \tag{64}$$

$$\kappa(\phi,\theta,0) = \kappa(_0(\phi,\theta)\ , \tag{65}$$

where Δ_s is the Laplace Beltrami operator. The variables ϕ,θ are the place coordinate on the sphere. And κ_0 is the starting boundary condition.

The boundary conditions on the edge of the sphere w have the following conditions:

$$\frac{\partial\kappa(\phi,\theta,t)}{\partial t} = \Delta_s\kappa(\phi,\theta,t) \tag{66}$$

$$\kappa(\phi,\theta,0) = \kappa_0(\phi,\theta)\ , \tag{67}$$

where Δ_s is the Laplace Beltrami operator. The variables ϕ,θ are the place coordinates on the sphere. And κ_0 is the starting boundary condition. The variable t will be used as a scaling variable in the same that the variable σ was used in the previous section. The behavior of the square of the gradient of the solution integrated over the entire sphere is determined for the limit of t going to 0.

The function $\kappa(\theta,\phi,t)$ can be described using the set of spherical harmonics since this is a complete set of orthonormal functions. This gives when filled into Equation (84)

$$\kappa(\theta,\phi,t) = \sum_{l=0}^{\infty}\sum_{m=0}^{l} A_{l,m}(t)Y_l^m(\theta,\phi) \tag{68}$$

with $A_{l,m}(t)$ a function based on l,m and t. Furthermore using the following property

$$\Delta_s Y_l^m = -l(l+1)Y_l^m$$

Equation (83) changes into

$$\kappa(\theta,\phi,t) = \sum_{l=0}^{\infty}\sum_{m=0}^{l} -l(l+1)A_{l,m}(t)\ Y_l^m(\theta,\phi)\ . \tag{69}$$

Solving this ODE gives

$$\kappa(\theta,\phi,t) = \sum_{l=0}^{\infty}\sum_{m=0}^{l} A_{0l,m}e^{-l(l+1)t}\ Y_l^m(\theta,\phi)\ . \tag{70}$$

To find $A_{0_{l,m}}$ solve

$$A_{0_{l,m}} = \int_0^{2\pi}\int_0^{\pi} Y_l^m(\theta,\phi)\kappa_0(\theta,\phi)\sin\theta d\theta d\phi\ . \tag{71}$$

Solving this for

$$\kappa_0(\theta,\phi) = \frac{\delta(\theta)\delta(\phi)}{\sin\theta}$$

gives

$$A_{0l,0} = \frac{1}{2} * \sqrt{\frac{1+2l}{pi}} \quad \text{and} \quad A_{0l,m} = 0 \text{ for } \quad m \neq 0. \tag{72}$$

Since all the factors $m \neq 0$ are zero, the function w is no longer dependent on ϕ. So the solution to the boundary condition for a specific t are

$$\kappa(\theta, t) = \sum_{l=0}^{\infty} \frac{1}{2} * \sqrt{\frac{1+2l}{\pi}} e^{-l(l+1)t} r^l Y_l^0(\theta) \tag{73}$$

Now $A_l(t)$ is set to $A_{l,0}(t)$ which means that

$$A_l(t) = \frac{1}{2} * \sqrt{\frac{1+2l}{\pi}} e^{-l(l+1)t} \ ,$$

so

$$\kappa(\theta, t) = \sum_{l=0}^{\infty} A_l(t) r^l Y_l^0(\theta) \ . \tag{74}$$

To determine the total moment given to the system the total force applied along the z-axis has to be determined. This is done in the same way as in Equation(22)

$$M = M_z = \int_0^{2\pi} \int_0^{\pi} \kappa(\theta, t) \cos(\theta) \sin(\theta) d\theta d\phi. \tag{75}$$

The limit for $t \to 0$ of M is

$$\lim_{t \to 0} M = 1, \tag{76}$$

since

$$\forall_{\epsilon > 0} \exists_{t_0 > 0} | \ \ |M - 1| < \epsilon. \tag{77}$$

This is proven in the following paragraph, but a few other statements have to be proven before Equation (76) can be proven. Using the relation that

$$\int_0^{2\pi} \int_0^{\pi} \kappa(\theta, t) \sin(\theta) d\theta d\phi = \int_0^{2\pi} \int_0^{\pi} \kappa(\theta, 0) \sin(\theta) d\theta d\phi = 1 \tag{78}$$

and that the function $\kappa(\theta, t_0)$ is a decreasing function. Meaning that for

$$\forall_{t_0 \geq 0} \forall_{0 \leq \theta^* \leq \pi} \forall_{\theta^* \leq \tilde{\theta} \leq \pi} | \ \kappa(\tilde{\theta}, t_0) \leq \kappa(\theta^*, t_0). \tag{79}$$

And since for $\theta^* > 0$ the function $\kappa(\theta^*, t)$ as a function of t is a continuous positive function with $\kappa(\theta^*, 0) = 0$, the following is true:

$$\forall_{\epsilon > 0} \forall_{\theta^* > 0} \exists_{t_0 > 0} | \kappa(\theta^*, t_0) < \epsilon. \tag{80}$$

An upper bound for the value $|M - 1|$ as a function of t is set. In the following equation α is introduced with the conditions that $0 < \alpha < \pi$

$$\begin{aligned}
|M - 1| &= | \int_0^{2\pi} \int_0^{\pi} \kappa(\theta, t) \cos(\theta) \sin(\theta) d\theta d\phi - \int_0^{2\pi} \int_0^{\pi} \kappa(\theta, t) \sin(\theta) d\theta d\phi | \\
&= \int_0^{2\pi} \int_0^{\pi} \kappa(\theta, t) | \cos(\theta) - 1 | \sin(\theta) d\theta d\phi \\
&= \int_0^{2\pi} \int_0^{\alpha} \kappa(\theta, t) | \cos(\theta) - 1 | \sin(\theta) d\theta d\phi + \int_0^{2\pi} \int_{\alpha}^{\pi} \kappa(\theta, t) | \cos(\theta) - 1 | \sin(\theta) d\theta d\phi \\
&\leq \int_0^{2\pi} \int_0^{\alpha} \kappa(\theta, t) | \cos(\alpha) - 1 | \sin(\theta) d\theta d\phi + \int_0^{2\pi} \int_{\alpha}^{\pi} \kappa(\theta, t) \sin(\theta) d\theta d\phi \\
&\text{using Equation (79) and (78)} \\
&\leq | \cos(\alpha) - 1 | + \int_0^{2\pi} \int_{\alpha}^{\pi} \kappa(\alpha, t) \sin(\theta) d\theta d\phi \\
&\leq | \cos(\alpha) - 1 | + 4\pi \kappa(\alpha, t)
\end{aligned} \tag{81}$$

Choose α in such a way that

$$|\cos(a) - 1| < \frac{\epsilon}{2} \tag{82}$$

and choose t_0 using Equation (80) such that $\kappa(a, t_0) < \frac{\epsilon}{8\pi}$, with this Equation (77) is satisfied so Equation (76) is proven.

The general solution to Equation (56) is equal to Equation (13

$$p(r, \phi, \theta) = \sum_{l=0}^{\infty} \sum_{m=0}^{l} (A_l r^l + B_l r^{-l-1}) Y_l^m(\theta, \phi) \tag{83}$$

and with azimuthal symmetry and the condition that the solution must be real and also be harmonic at $r = 0$, the general solution is

$$p(r, \theta, \phi) = \sum_{l=0}^{\infty} A_l r^l P_l(\cos(\theta)) \ . \tag{84}$$

To determine ∇u the derivative of u to r,θ and ϕ is calculated. Since u is not dependent on ϕ the derivatives to ϕ are equal to zero. This gives

$$\nabla p(r, \theta, \phi, t) = \sum_{l=0}^{\infty} A_l(t)(l r^l Y_l^0(\theta) \overline{e}_r) + \sqrt{l(l+1)} e^{-i\phi} P_l^1(\cos(\theta)) \overline{e}_\theta \tag{85}$$

with P_l^1 the Legendre function normalized such that

$$\int_0^\pi P_l^1(\cos(\theta)) P_k^1(\cos(\theta)) \sin(\theta) d\theta = \frac{1}{2\pi} \delta_{lk} \tag{86}$$

Just as in the case of the half space, the behaviour of the total kinetic energy, E_{kin} is determined with the integral of $|\nabla u|^2$. This gives

$$\begin{aligned} E_{kin} &= \int_0^1 \int_0^{2\pi} \int_0^\pi |\nabla p(r, \theta, \phi, t)|^2 r^2 \sin(\theta) d\theta d\phi dr \\ &= \int_0^1 \int_0^{2\pi} \int_0^\pi \sum_{l=0}^{\infty} \sum_{k=0}^{\infty} A_l(t) A_k(t) (lk\} Y_l^0(\theta) Y_k^0(\theta) \\ &+ \sqrt{l(l+1)k(k+1)} P_l^1(\theta) P_k^1(\theta)) r^{l+k} \sin(\theta) d\theta d\phi dr \end{aligned} \tag{87}$$

Since this can be seen as an in product in L^2 with a base orthonormal base of spherical harmonics, the integral and sums can be interchanged so that

$$\begin{aligned} E_{kin} &= \sum_{l=0}^{\infty} \sum_{k=0}^{\infty} \int_0^1 \int_0^{2\pi} \int_0^\pi A_l(t) A_k(t) (lk\} Y_l^0(\theta) Y_k^0(\theta) \\ &\quad + \sqrt{l(l+1)k(k+1)} P_l^1(\theta) P_k^1(\theta)) r^{l+k} \sin(\theta) d\theta d\phi dr \\ &= \sum_{l=0}^{\infty} \sum_{k=0}^{\infty} \int_0^1 A_l(t) A_k(t) (lk \ r^{l+k} \delta_{lk} + r^{l+k} \sqrt{l(l+1)k(k+1)} \delta_{lk}) dr \\ &= \sum_{l=0}^{\infty} \int_0^1 A_l(t)^2 (2l^2 + 1 \ r^{2l}) dr \\ &= \sum_{l=0}^{\infty} A_l(t)^2 [l r^{2l+1}]_0^1 = \sum_{l=0}^{\infty} \frac{1}{4} \frac{1+2l}{\pi} e^{-2l(l+1)t} l \end{aligned} \tag{88}$$

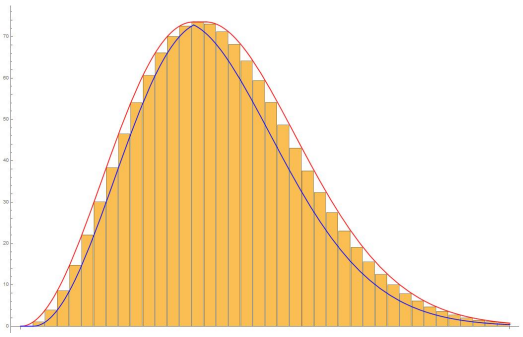

Figure 17: $F^+(l)$ in red and $F^-(l)$ in blue shown as upper and lower bounds for $\sum_{l=0}^{\infty} l^2 e^{-l^2 t}$ which is shown in yellow rectangles with t=0.005

For this sum an upper and lower bound are used to be able to determine itsbehaviour. The following holds

$$\frac{1}{2\pi}\sum_{l=0}^{\infty} l^2 e^{-l^2 t} \leq \sum_{l=0}^{\infty} \frac{1}{4}\frac{l(1+2l)}{\pi} e^{-2l(l+1)t} \leq \frac{1}{\pi}\sum_{l=0}^{\infty} l^2 e^{-l^2 t}. \tag{89}$$

To determine the sum $\sum_{l=0}^{\infty} l^2 e^{-l^2 t}$ an upper and lower bound are determined using the function

$$f(l) = l^2 e^{-l^2 t}. \tag{90}$$

For $l \geq 0$ the function is continuous. Furthermore it is increasing for $l \leq \frac{1}{\sqrt{t}}$ and decreasing from $l \geq \frac{1}{\sqrt{t}}$. Now an upper and lower bound can be determined for $\sum_{l=0}^{\infty} l^2 e^{-l^2 t}$ with F^+ the upper limit and F^- the lower limit functions. Set for $t < 1$:

$$F^+(l) = \begin{cases} l^2 e^{-l^2 t} & l \leq \frac{1}{\sqrt{t}} \\ \frac{1}{t} e^{-1} & \frac{1}{\sqrt{t}} \leq l \leq \frac{1}{\sqrt{t}} + 1 \\ (l-1)^2 e^{-(l-1)^2 t} & l \geq \frac{1}{\sqrt{t}} + 1 \end{cases}$$

$$F^-(l) = \begin{cases} 0 & l \leq 1 \\ (l-1)^2 e^{-(l-1)^2 t} & 1 \leq l \leq \frac{1}{\sqrt{t}} \\ (l+1)^2 e^{-(l+1)^2 t} & l \geq \frac{1}{\sqrt{t}} \end{cases}$$

Now the following is true:

$$F^-(l) \leq f(\lfloor l \rfloor) \leq F^+(l). \tag{93}$$

Integrating these three function over l from 0 to ∞ gives

$$\int_0^{\infty} F^-(l)dl \leq \int_0^{\infty} f(\lfloor l \rfloor)dl \leq \int_0^{\infty} F^+(l)dl. \tag{94}$$

$$\int_0^{\infty} l^2 e^{-l^2 t} - 2\frac{e^{-1}}{t} \leq \int_0^{\infty} F^-(l)dl \leq \sum_{l=0}^{\infty} l^2 e^{-l^2 t} \leq \int_0^{\infty} F^+(l)dl = \int_0^{\infty} l^2 e^{-l^2 t} + \frac{e^{-1}}{t}. \tag{95}$$

The integral $\int_0^{\infty} l^2 e^{-l^2 t}$ can be solved using the inverse product rule with

$$\int_0^{\infty} F(l)G'(l)dl = [F(l)G(l)]_0^{\infty} - \int_0^{\infty} F'(l)G(l)dx\ . \tag{96}$$

Set

$$F(l) = l \text{ and } G'(l) = le^{-l^2t}. \tag{97}$$

Then

$$F'(l) = 1 \text{ and } G(l) = -\frac{1}{2t}e^{-l^2t}. \tag{98}$$

Further more by substituting $u = l\sqrt{t}$ it follows that

$$\int F'(l)G(l)_0^\infty dl = \int_0^\infty -\frac{1}{2t}e^{-l^2t}dl = -\frac{1}{2t^{\frac{3}{2}}}\int_0^\infty e^{-u^2}du = -\frac{\sqrt{\pi}}{4t^{\frac{3}{2}}}erf(l\sqrt{t}).$$

This means that

$$\int_0^\infty l^2e^{-l^2t}dl = [-\frac{l}{2t}e^{-l^2t} + \frac{\sqrt{\pi}}{4t^{\frac{3}{2}}}erf(l\sqrt{t})]_0^\infty = \frac{\sqrt{\pi}}{4t^{\frac{3}{2}}}, \tag{99}$$

Filling in this result from Equation (99) into Equation (95) while multiplying by $t^{\frac{3}{2}}$ and taking the limit of $\lim_{t\to 0}$ gives

$$\lim_{t\to 0}(\frac{\sqrt{\pi}}{4t^{\frac{3}{2}}} - 2\frac{e^{-1}}{t})t^{\frac{3}{2}} \leq \lim_{t\to 0}t^{\frac{3}{2}}\sum_{l=0}^{\infty} l^2e^{-l^2t} \leq (\lim_{t\to 0}\frac{\sqrt{\pi}}{4t^{\frac{3}{2}}} + \frac{e^{-1}}{t})t^{\frac{3}{2}} \tag{100}$$

$$\frac{\sqrt{\pi}}{4} \leq \lim_{t\to 0}t^{\frac{3}{2}}\sum_{l=0}^{\infty} l^2e^{-l^2t} \leq \frac{\sqrt{\pi}}{4} \tag{101}$$

So

$$\lim_{t\to 0}t^{\frac{3}{2}}\sum_{l=0}^{\infty} l^2e^{-l^2t} = \frac{\sqrt{\pi}}{4} \tag{102}$$

Using the result from Equation (102) in Equation (89) while again multiplying by $t^{\frac{3}{2}}$ and taking the the limit of $\lim_{t\to 0}$ the following follows:

$$\frac{1}{8\sqrt{\pi}} \leq \lim_{t\to 0}t^{\frac{3}{2}}\sum_{l=0}^{\infty}\frac{1}{4}\frac{l(1+2l)}{\pi}e^{-2l(l+1)t} \leq \frac{1}{4\sqrt{\pi}} \tag{103}$$

So the sum $\sum_{l=0}^{\infty} t^{\frac{3}{2}}\frac{1}{4}\frac{l(1+2l)}{\pi}e^{-2l(l+1)t}$ is bounded for $\lim_{t\to 0}$ while it is also a positive sum. This means that the limit must exist and since it is bounded from below by $\frac{1}{8\sqrt{\pi}}$ the limit is non zero. This means that

$$\lim_{t\to 0}t^{\frac{3}{2}}E_{kin} = E_0 \tag{104}$$

with $E_0 > 0$. To determine the asymptotic behaviour of the deformation energy the translation energy, E_{trans} is subtracted from the total kinetic energy.

$$\begin{aligned}\lim_{t\to 0}t^{\frac{3}{2}}E_{def} &= \lim_{t\to 0}t^{\frac{3}{2}}(E_{kin} - E_{trans}) = \lim_{t\to 0}E_0(-t^{\frac{3}{2}}\frac{M^2}{2m}) \\ &= \lim_{t\to 0}E_0(-t^{\frac{3}{2}}\frac{1}{2m}) = E_0\end{aligned} \tag{105}$$

$$\lim_{t\to 0}\sum_{l=0}^{\infty} l^2e^{-l^2t} = \lim_{t\to 0}\frac{\sqrt{\pi}}{4t^{\frac{3}{2}}} \tag{106}$$

since σ scales with t as

$$\sigma \propto \sqrt{t}, \tag{107}$$

the following is true when taking the limit of $\sigma \to 0$:

$$\lim_{t\to 0}\sigma^3E_{def} = E_1 \tag{108}$$

with E_1 a non zero constant.

This result is similar to the result on the half space of the previous section. The difference however is that on the sphere the relation between the gradient squared and scaling of the problem is only valid when taking the limit of the scaling to 0 whereas for the half space any scaling was valid. This is due to the fact that on a sphere the radius is also a unit of space.

9 Conclusion

The physics of the laser tin droplet interaction is translated into a pressure profile problem. This problem is mathematically solved using spherical harmonics for any boundary condition. This mathematical model is then used to determine the pressure and velocity field through a droplet after the laser pulse. The calculations with data from ARCNL show that for higher energies the ratio $\frac{E_{def}}{E_{kin}}$ decreases, this decrease is explained using experimental image of the plasma cloud. For a larger focus length of the laser this ratio also decreases. This is caused by the fact that the forces on the droplet spread out more evenly for higher focus lengths which cause less outwards motion in the droplet. Furthermore it was shown that for an off set Gaussian shaped laser profiles the off set had only a small effect on the ratio $\frac{E_{def}}{E_{kin}}$. Furthermore the behaviour of the energy ratio for small focus lengths, $\sigma << 1$ was analytically determined to approach 1.

$$\frac{E_{def}}{E_{kin}} \propto \frac{\sigma^{-3}}{\sigma^{-3}+1}. \tag{109}$$

Besides the actual laser profiles that were discussed in this report, the method using spherical harmonics to determine the properties of the deformation and translation of a droplet can be used on all kind of droplets for all kind of laser beam profiles.

10 Discussion

The main point of this report has been to look at the behaviour of tin droplet during the laser pulse and the period shortly afterward were the droplet is still approximately spherical but lacks information on how these beginning features of the deformation of the tin droplet have an effect when it is no transformed into a thin sheet. To be able to determine the behaviour of the tin droplet for a larger time scale the pressure and velocity fields have to be determined for the deforming shape and the surface tension has to be account for too. The velocity profiles created in this report could serve as the boundary condition for further research. Furthermore, the error between the boundary condition and the approximation is still high in Chapter 6.2 and more computation time would provide better results. The laser-plasma interaction has also been simplified and the results in this report could be improved by providing a better conversion from laser intensity to pressure. Using the plasma simulations from [5] on the pressure profiles discussed in Chapter 6 and Chapter 7 could provide some insightfull information about these different laser profiles.
Further research could use the methods created in this report to determine the behaviour of the tin droplet for different laser beam profiles to find more effective ways of deforming droplets.

References

[1] Gelderblom, Hanneke, Henri Lhuissier, Alexander L. Klein, Wilco Bouwhuis, Detlef Lohse, Emmanuel Villermaux, and Jacco H. Snoeijer **2016** *Drop deformation by laser-pulse impact.*. Journal of fluid mechanics, 794, 676-699. doi:10.1017/jfm.2016.182

[2] Gelderblom, Hanneke and Oscar Versolato **2017** *Laserschieten op tindruppels.* (Dutch) Tijdschrift voor Natuurkunde, November, 376-379.

[3] Reijers, Sten A., Dmitry Kurilovich, Francesco Torretti, Hanneke Gelderblom, and Oscar O. Versolato, **2018** *Laser-to-droplet alignment sensitivity relevant for laser-produced plasma sources of extreme ultraviolet light.* Journal of Applied Physics 124, 013102, doi: 10.1063/1.5026950, doi online version 10.1063/1.5026950.

[4] Courant, Richard; Hilbert, David **1953** *Methods of Mathematical Physics, Volume 1.* New York: Interscience Publischer, Inc. Doi: aip.scitation.org/doi/full/10.1063/1.5010899

[5] Kurilovich, D., Basko, M. M., Kim, D. A., Torretti, F., Schupp, R., Visschers, J. C and Versolato, O. O. **2018** *Power-law scaling of plasma pressure on laser-ablated tin microdroplets.*. Physics of Plasmas, 25(1), 012709.

[6] Klein, A. L., Bouwhuis, W., Visser, C. W., Lhuissier, H., Sun, C., Snoeijer, J. H., and Gelderblom, H. **2015** *Drop shaping by laser-pulse impact.* Physical review applied, 3(4), 044018.

[7] M. M. Basko, V. G. Novikov, and A. S. Grushin**2015** *On the structure of quasi-stationary laser ablation fronts in strongly radiating plasmas.* Phys. Plasmas 22, 053111

[8] Klein, A. L. **(2017).** *Laser impact on flying drops* Enschede DOI: 10.3990/1.9789036543422

[9] Mizoguchi, H., Abe, T., Watanabe, Y., Ishihara, T., Ohta, T., Hori, T., and Wakabayashi, O. **(2010).** *First generation laser-produced plasma source system for HVM EUV lithography. In Extreme Ultraviolet (EUV) Lithography* (Vol. 7636, p. 763608). International Society for Optics and Photonics.